minerals

MDPI

Article

In Situ U–Th–Pb Dating of Parisite: Implication for the Age of Mineralization of Colombian Emeralds

Uwe Altenberger [1], Yamirka Rojas-Agramonte [2,3,*], Yueheng Yang [4], Jimmy Fernández-Lamus [5], Tobias Häger [3], Christina Guenter [1], Alejandra Gonzalez-Pinzón [6], Felipe Charris-Leal [6] and Julia Artel [1]

[1] Institute of Geosciences, University of Potsdam, Karl-Liebknecht Str. 24-25, House 27, D-14476 Potsdam-Golm, Germany
[2] Institut für Geowissenschaften, Christian-Albrechts-Universität zu Kiel, Ludewig-Meyn-Straße 10, D-24118 Kiel, Germany
[3] Institut für Geowissenschaften, Johannes Gutenberg-Universität Mainz, J.-J. Becherweg 21, D-55099 Mainz, Germany
[4] State Key Laboratory of Lithospheric Evolution, Institute of Geology and Geophysics, Chinese Academy of Sciences, No. 19, Beitucheng Western Road, Chaoyang District, Beijing 100029, China
[5] Departamento de Geosciencias, Universidad Nacional de Colombia, Bogotá 11001, Colombia
[6] Natural Colombia Mineral SAS, Bogotá, Colombia
* Correspondence: yamirka.rojas@ifg.uni-kiel.de

Abstract: Parisite-Ce ($Ca(Ce,La)_2(CO_3)_3F_2$) is a rare-earth (REE) fluorocarbonate mineral first described from the world-famous emerald mines of the Muzo district, Boyacá Province, Colombia. Four samples of parisite-Ce collected from outcrops near Muzo have been geochemically studied and dated using the in situ laser ablation U–Th–Pb method. Our study shows that the REE abundance of parisite is controlled by the leaching of the wall rocks (black schist). Furthermore, we show that the parisite-Ce crystals formed in textural equilibrium with the emeralds, suggesting a similar time of crystallization. Our analysis demonstrates the capability of parisite as a geochronometer and shows that precise and accurate U–Th–Pb ages can be obtained from parisite after common ^{207}Pb correction. A higher precision date was obtained with the Th–Pb ratio rather than with the U–Pb ratio because of the relatively higher content of Th than U in the samples. The samples yielded ^{208}Th–^{232}Pb ages ranging from ~47 to 51 Ma. The new ages are ~10 Ma older than previously reported Ar–Ar ages and ~10 Ma younger than previously reported Rb/Sr ages. These results will have significant implications for understanding the timing of mineralization and crystallization of emerald deposits in Colombia. Furthermore, this study opens new avenues for dating similar deposits worldwide.

Keywords: geochronology; U–Th–Pb dating; parisite; calcite; emeralds; Muzo; Eastern Cordillera; Colombia

Citation: Altenberger, U.; Rojas-Agramonte, Y.; Yang, Y.; Fernández-Lamus, J.; Häger, T.; Guenter, C.; Gonzalez-Pinzón, A.; Charris-Leal, F.; Artel, J. In Situ U–Th–Pb Dating of Parisite: Implication for the Age of Mineralization of Colombian Emeralds. *Minerals* **2022**, *12*, 1232. https://doi.org/10.3390/min12101232

Academic Editor: Frederick Lin Sutherland

Received: 6 July 2022
Accepted: 22 September 2022
Published: 28 September 2022

1. Introduction

For much of recorded history, Colombia has produced the largest and highest-quality emerald crystals in the world. More than 200 emerald deposits and occurrences in the country are located in two narrow belts on either side of the Eastern Cordillera (Figure 1). The two mineralization belts are located some 80 km apart. In the western emerald belt (western zone) are the districts of Peñas Blancas, Coscuez, Muzo and Yacopí, while in the eastern emerald belt (eastern zone) are the major mining districts of Gachalá, Chivor and Macanal (Figure 1). Colombian emeralds are unique in their genesis and differ from other emerald deposits in the world, by the fact that they are located in sedimentary to low-grade metamorphic rocks [1] (Figure 1). Several non-magmatic genetic models have been proposed for the formation of the emerald deposits. The most accepted is the epigenetic hydrothermal–sedimentary model of Giuliani et al. [2], in which magmatic processes as suggested by Oppenheim [3] are not necessary.

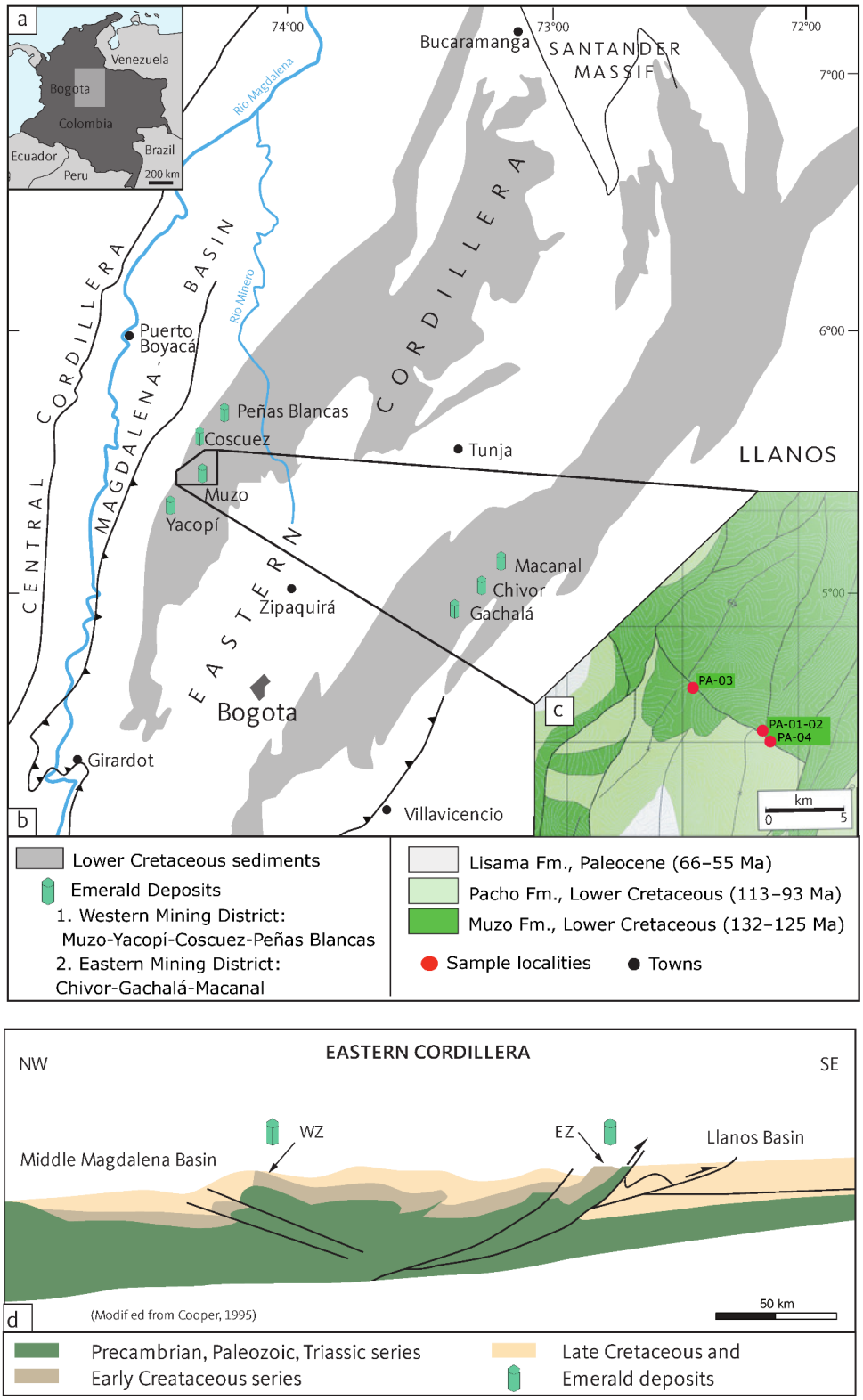

Figure 1. (**a**,**b**) Simplified map showing the major tectonic provinces of northwestern Colombia and its location in South America (inset a). (**c**) Detailed geological map of the sample area with sample localities. (**d**) Cross-section through the bivergent fold and thrust belt of the Eastern Cordillera. The over-thrusting of the two foreland basins containing the emerald deposits is shown: western zone (WZ, Muzo, Coscuez, Yacopí and Peñas Blancas) and eastern zone (EZ; Chivor, Gachalá and Macanal). (**a**,**b**) Modified after Branquet et al. (1999) and Cooper (1995).

Emerald deposits in the eastern zone (Figure 1) are estimated to be 61 million years old and are associated in time with a Cretaceous extensional tectonic regime [4,5]. The deposits in the western zone have been dated at 32 and 35–38 million years and are associated with tear and thrust faults which predate the main uplift of the mountain range during the mid-Miocene [6]. Romero-Ordoñez et al. [5] obtained ages ranging from 61 to 67 Ma using the Rb–Sr isotopic method for emeralds from both the eastern and western zones. $^{40}Ar/^{39}Ar$ ages reveal 38–32 Ma in muscovite [6]. In addition, an unpublished BSc showed similar muscovite ages for the western zone (Muzo district), indicating two stages of hydrothermal activity around 62 Ma and 30 Ma [7]. Therefore, the published results so far indicate that the age of emerald formation is poorly constrained.

Parisite-$CaCe_2(CO_3)_3F_2$ is a rare-earth fluorocarbonate with cerium, lanthanum or neodymium as the dominant rare-earth element. The mineral crystalizes in the monoclinic system and was first described in the emerald mines of the Muzo district by Lavinio de Medici-Spada, a poet and mineralogist, and J.J. Paris in 1848 [8,9]. The parisite in the Muzo region is the Ce-type [10], and appears to have formed at the same time as the emeralds (Figure 2a,b). The fluorocarbonate also occurs as inclusions within the emeralds [11]; therefore, it is used as a mineral indicator for emerald crystallization [12]. Parisite is part of the bastnäsite group [13], where bastnäsite, $REE(CO_3)F$, and synchysite, $CaREE(CO_3)_2F$, represent the end members [14].The bastnäsite group minerals, including parisite, contain U and Th [14], and thus have potential to be used as geochronometers.

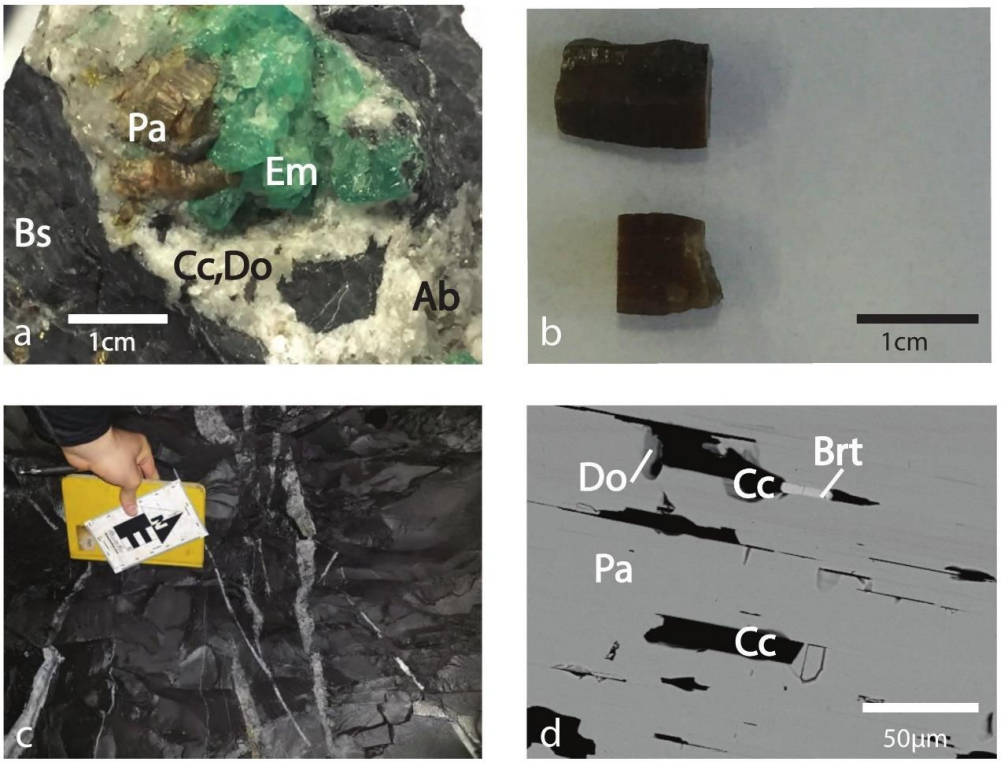

Figure 2. Parisite samples: (**a**) Parisite–emerald-bearing sample from Muzo; BS = black shale, Ab = albite, Pa = parisite, Cc = calcite, Do = dolomite, Brt = baryte. (**b**) Photo showing two of the analyzed parisite crystals from sample PA-01. (**c**) Sample locality with carbonate-rich dikes cutting the bedding planes of black shales (PA-03). (**d**) Back-scattered electron image (BSE) of inclusions in parasite (baryte (light), calcite (black) and dolomite (grey)).

Recent studies by Artel et al. [15] and Zeug et al. [14] reveal the possible complex internal structure of the parisite crystals from the Muzo region. The mineral can be internally composed of polycrystalline aggregates and can also consist of various polytypic and polysomatic intergrowths of several fluorocarbonate phases of the bastnäsite group (La

Pita Mine [14]). In the present study, we show for the first time in situ U–Th–Pb dating of parisite from the Muzo district. In addition, we report in situ trace element and Sm–Nd isotope analysis in order to better understand and constrain the time and genesis of emerald mineralization in the western zone of the Eastern Cordillera.

2. Geological Setting and Emerald Formation

The Eastern Cordillera of Colombia constitutes the relic of an uplifted Cretaceous marine sedimentary basin with a unique tectono-sedimentary evolution ([16–18], Figure 1b). The emerald mineralization is hosted in Lower Cretaceous (135–116 Ma) sedimentary rocks composed of a thick succession of sandstone, limestone, black shale and evaporites [6,19,20]. The up to ten-kilometer-thick Cretaceous and overlying Eocene sediments were deposited in a back-arc basin, that is segmented into various sub-basins [17,18,21]. The subsidence of the basin has been explained as an early rifting phase in the Early Cretaceous, followed by a thermal decay after rifting in the Late Cretaceous [16,19]. Deposition was followed by fault inversion and overthrusting onto the Los Llanos basin in the east and the Magdalena basin to the west (Figure 1b,d; [18,19]).

The mineralization in each of the two flanks of the Eastern Cordillera is suggested to have occurred in two different tectonic settings [22] and ages [6,23,24]: In the eastern zone (Chivor area), emerald deposits formed during the Paleocene (61 Ma, $^{87}Rb/^{86}Sr$) in a thin-skinned extensional tectonic regime controlled by gravity-driven evaporite dissolution [6,22]. In the western zone (Muzo area), the emerald deposits are linked to listric faults and associated thrusts developed during an Eocene–Oligocene (structural data) compressional tectonic phase, prior to the major uplift of the Cordillera during the middle Miocene [22], supported by $^{40}Ar/^{39}Ar$ ages of 38–32 Ma [6]. However, Paleocene Rb–Sr ages of emeralds are similar for both zones, 61 Ma in the eastern zone and 67 Ma in the western zone (Rb/Sr in emeralds [6]), although the structures controlling emerald formation in the western zone are suggested to be Eocene–Oligocene in age [6,22].

Nevertheless, in both emerald zones, saline hydrothermal brines and their interaction with black shales are the major controls responsible for the origin of the epigenetic emerald-bearing systems [25]. Fluid inclusion studies [25] show the mixing of two chlorine-rich saline fluids that dominate both emerald zones, despite the differing ages. Whereas one fluid is Na-rich, coming from the solution of underlying halite beds, the other one is more Ca-rich, which is controlled by dissolution of anhydrite and/or by leaching of the wall rocks [25]. The strong influence of halite is due to the Lower Cretaceous salt deposits, locally exhumed during the Tertiary. Beryllium (Be) was transported in the form of Be-F complexes in a NaCl fluid and precipitated as emeralds after mixing with calcium brines causing the precipitation of fluorite and parisite [25].

The emerald deposits of the eastern zone (Chivor district) are hosted in Lower Cretaceous black shales (142–137 Ma) at the base of the Macanal series (137–132 Ma). According to [20,22], the deposits in the Chivor district formed in a series of siliceous or carbonated black shales, limestones and minor siltstones. Most emerald deposits of the Muzo district on the western flank of the Cordillera occur epigenetically in Lower Cretaceous (ca 132–127 Ma) carbonated black shales and the underlying dolomitic limestones (Rosablanca Formation). Minor deposits occur in Lower Cretaceous siliceous black shales and rarely in younger schists (ca 121–112 Ma) [20,22].

Emerald crystals are found in carbonate-, silicate-, pyrite-rich veins, pockets and extensional breccia, black graphite-rich shales and carbonate rocks (e.g., [3,9]). Although these mineralogical and geochemical parameters in both zones are basically the same, they differ in their structural relationship to the wall rocks [22]. In the western zone, the emerald deposits form after the fracturing and brecciation of the hanging wall rock sequence. In contrast, in the eastern zone, the hydrothermal fluids and evaporites are scattered along a regional-scale stratiform brecciated zone [22].

For the western zone, Giuliani et al. [2] describe two major phases of mineralization, which they correlate with two compressional tectonic stages. The first phase crys-

tallized albite, calcite, green mica (fuchsite) and pyrite, while the second phase formed calcite/dolomite, quartz, fluorite and emerald in the veins and breccias. Banks et al. [25] describe 3 stages of mineralization: the initial one, with fibrous calcite, pyrite 1, albite, quartz and green mica, a second one with rhombohedral calcite, dolomite, albite, pyrite 2 and kerogens, and a third one, with emeralds, pyrite 3 and parisite-Ce with REE—dolomite, fluorite and quartz. However, both studies indicate the growth of emerald and parisite in one stage. According to Banks et al. [25], the mineralizing fluids were derived from the interaction of low-salinity fluids with halite and anhydrite. Beryllium, chromium and vanadium were derived from the black shales. The rare-earth elements necessary to form parisite-Ce are also mainly leached from the black shales ([15] and present study).

Alonso-Perez et al. [26] compare the rare-earth element and incompatible trace element abundances of emeralds that have formed in different environments. They confirmed that the emerald deposits in Colombia or "type IIb emeralds" are generated in a sedimentary environment characterized by flat, crustal-normalized, REE patterns very similar to shales and loess (Figure 3). In contrast, magmatic-originated emeralds (Type Ia) show a steep negative slope, i.e., La_{crust}/Yb_{crust} of ca. 0.3 (e.g., Madagascar and Brazil).

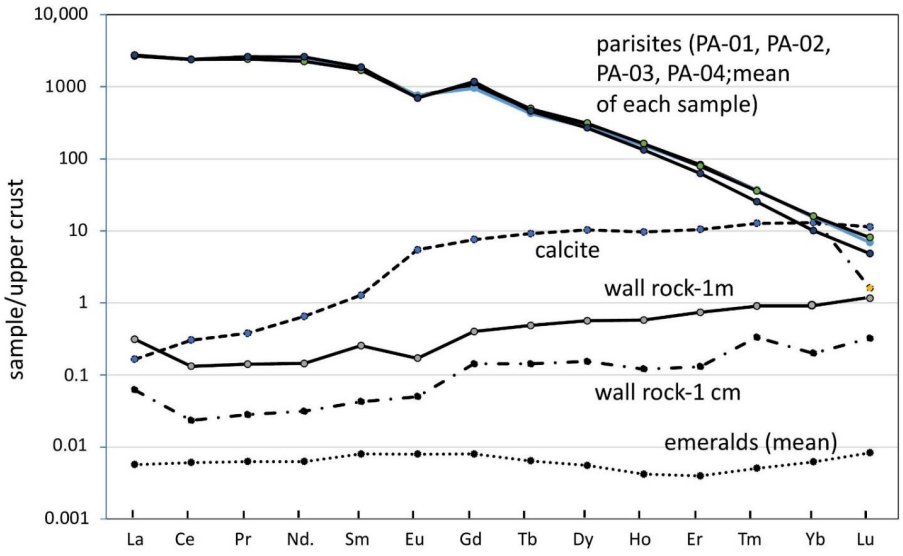

Figure 3. Mean REE concentrations of four parisites (mean of 13–23 samples) and their coexisting minerals and wall rock system. REE are upper crustal-normalized (Rudnick et al., 2003).

3. Analytical Methods

The four parisite-Ce samples were collected in outcrops (PA-01, PA-02) and mines (PA-03, PA-04) near Muzo (Figure 1c) and are part of emerald–parisite–calcite–albite-veins, hosted in graphite-bearing shales (Figure 2a–c). In general, the sampled localities are characterized by the presence of hydraulic breccias, mainly massive calcite–albite mineralization cutting through the bedding with evidence of hydrothermal alteration (Figure 2c). The bed rock contained crystals of pyrite and iron oxides, with minor presence of calcite vein with albite, malachite/azurite.

The parisite crystals were mechanically broken out of the rock and polished for thin sections. They were further analyzed with a Jeol Superprobe JXA-8200 electron microprobe (EMP), and by a scanning electron microscope Jeol JSM-651 (SEM) with an Oxford Inca X-act energy-dispersive spectrometer (EDX) at the University of Potsdam. For the EMP analyses, artificial standards from the Smithsonian Institute and natural monazite were used. Rare-earth element (REE) analyses of the wall rock and coexisting calcite were performed by inductively coupled plasma optical emission spectrometry (ICP-OES) with an ICP 5100 from Agilent at the University of Potsdam and by inductively coupled plasma mass spectrometry Agilent 7500a Q-ICP-MS at the State Key Laboratory, Beijing (supplementary material and Table 1).

Table 1. U–Th–Pb isotope data of parisite using laser ablation.

	ppm	ppm	ppm		Ratio		Ratio		Ratio		Ratio		Ratio		Age (Ma)	
															207Pb Corr.	
	Pb	Th	U	Th/U	U238/Pb206	1s	Pb207/Pb206	1s	Pb207/U235	1s	Pb206/U238	1s	Pb208/Th232	1s	Pb208/Th232	1s
PA-01-01	9.4	7360	11.9	617	75.9	1.8	0.0333	0.0025	0.0605	0.0043	0.01318	0.00031	0.00236	0.00004	47.7	0.8
PA-01-02	9.3	7774	12.3	631	73.3	1.9	0.0341	0.0028	0.0640	0.0051	0.01364	0.00035	0.00238	0.00004	48.1	0.8
PA-01-03	8.9	7452	11.9	629	51.3	1.4	0.2738	0.0104	0.7347	0.0233	0.01948	0.00052	0.00238	0.00004	48.0	0.9
PA-01-04	9.5	7360	11.8	623	71.0	1.9	0.0370	0.0030	0.0717	0.0056	0.01408	0.00037	0.00237	0.00004	47.9	0.8
PA-01-05	9.2	6969	11.1	627	73.2	1.9	0.0333	0.0029	0.0626	0.0053	0.01366	0.00035	0.00238	0.00004	48.1	0.8
PA-01-06	8.5	6486	10.8	599	72.2	1.8	0.0379	0.0028	0.0724	0.0052	0.01386	0.00034	0.00238	0.00004	48.0	0.8
PA-01-07	9.9	7052	10.7	658	65.2	1.8	0.0304	0.0030	0.0643	0.0062	0.01534	0.00043	0.00240	0.00004	48.4	0.9
PA-01-08	10.2	7298	10.9	670	68.6	1.9	0.0282	0.0031	0.0567	0.0061	0.01457	0.00041	0.00241	0.00004	48.6	0.9
PA-01-09	8.6	6357	10.2	621	69.8	1.9	0.0283	0.0028	0.0559	0.0054	0.01432	0.00039	0.00235	0.00004	47.4	0.9
PA-01-10	9.4	6831	10.7	637	69.8	2.0	0.0483	0.0039	0.0955	0.0073	0.01433	0.00041	0.00238	0.00004	48.0	0.9
PA-01-11	9.0	6555	10.9	604	56.7	1.5	0.1852	0.0075	0.4498	0.0159	0.01763	0.00046	0.00239	0.00004	48.1	0.9
PA-01-12	8.4	7222	11.5	627	66.7	2.0	0.0683	0.0051	0.1411	0.0100	0.01499	0.00045	0.00228	0.00004	46.1	0.9
PA-02-01	4.2	4853	8.4	578	117.6	4.6	0.0668	0.0071	0.0781	0.0079	0.00850	0.00033	0.00253	0.00005	51.1	1.1
PA-02-02	4.8	6302	8.7	728	107.9	4.1	0.0448	0.0057	0.0572	0.0070	0.00927	0.00035	0.00242	0.00005	49.0	1.0
PA-02-03	5.6	7935	8.2	965	99.3	3.6	0.0482	0.0053	0.0669	0.0071	0.01007	0.00037	0.00234	0.00005	47.3	1.0
PA-02-04	4.5	6118	8.1	751	114.7	4.5	0.0543	0.0065	0.0652	0.0075	0.00872	0.00034	0.00248	0.00005	50.1	1.1
PA-02-05	4.2	5773	8.7	665	113.6	4.4	0.0802	0.0079	0.0972	0.0090	0.00880	0.00034	0.00248	0.00005	50.1	1.1
PA-02-06	3.8	5382	7.9	680	114.7	4.5	0.0501	0.0070	0.0602	0.0081	0.00872	0.00034	0.00256	0.00005	51.6	1.1
PA-02-07	4.6	6716	8.6	781	114.3	4.4	0.0609	0.0072	0.0734	0.0084	0.00875	0.00034	0.00252	0.00005	50.8	1.1
PA-02-08	4.5	6923	8.5	812	110.3	4.3	0.0800	0.0076	0.0999	0.0089	0.00907	0.00035	0.00251	0.00005	50.6	1.1
PA-02-09	4.6	7015	7.2	978	102.5	4.1	0.0516	0.0068	0.0694	0.0088	0.00976	0.00039	0.00239	0.00005	48.3	1.0
PA-02-10	4.1	6095	8.4	725	118.5	4.8	0.0693	0.0075	0.0806	0.0083	0.00844	0.00034	0.00248	0.00005	50.0	1.1
PA-02-11	4.3	5612	8.1	690	111.1	5.6	0.0589	0.0094	0.0730	0.0111	0.00900	0.00045	0.00256	0.00006	51.6	1.2
PA-02-12	4.2	5451	8.3	656	111.2	4.3	0.0685	0.0069	0.0849	0.0081	0.00899	0.00035	0.00254	0.00005	51.3	1.1
PA-02-13	4.0	5359	8.0	672	117.0	4.9	0.0582	0.0079	0.0686	0.0089	0.00855	0.00036	0.00254	0.00005	51.3	1.1
PA-02-14	3.7	6279	8.1	771	122.7	5.0	0.0496	0.0076	0.0558	0.0083	0.00815	0.00033	0.00240	0.00005	48.5	1.0
PA-02-15	3.8	6578	9.1	721	123.3	4.9	0.0577	0.0071	0.0645	0.0076	0.00811	0.00032	0.00250	0.00005	50.4	1.1
PA-02-16	4.0	7153	9.0	795	118.6	4.5	0.0753	0.0076	0.0875	0.0084	0.00843	0.00032	0.00249	0.00005	50.4	1.1
PA-02-17	4.1	9108	9.4	971	118.3	4.6	0.0602	0.0069	0.0701	0.0078	0.00845	0.00033	0.00250	0.00005	50.5	1.1
PA-03-01	4.9	2234	13.0	172	83.8	2.9	0.2273	0.0120	0.3738	0.0166	0.01194	0.00041	0.00254	0.00006	51.3	1.1
PA-03-02	5.0	2338	15.0	155	98.7	3.0	0.1264	0.0069	0.1765	0.0086	0.01013	0.00031	0.00251	0.00005	50.7	1.0
PA-03-03	2.1	966	11.3	86	97.3	3.1	0.1445	0.0084	0.2046	0.0106	0.01028	0.00033	0.00248	0.00006	50.0	1.2
PA-03-04	5.6	2510	16.6	151	84.7	2.7	0.2152	0.0102	0.3502	0.0141	0.01181	0.00037	0.00255	0.00005	51.6	1.1
PA-03-05	4.6	2072	13.4	155	87.0	2.5	0.2577	0.0106	0.4084	0.0142	0.01150	0.00033	0.00256	0.00005	51.6	1.0
PA-03-06	1.3	543	10.2	53	97.7	3.8	0.1603	0.0114	0.2261	0.0140	0.01024	0.00040	0.00253	0.00008	51.0	1.6
PA-03-07	6.5	3003	15.7	192	107.4	3.3	0.0566	0.0047	0.0725	0.0057	0.00931	0.00029	0.00251	0.00005	50.7	1.0
PA-03-08	5.1	2378	16.0	149	107.6	3.0	0.0717	0.0043	0.0918	0.0051	0.00929	0.00026	0.00248	0.00005	50.1	1.0

Table 1. *Cont.*

	ppm	ppm	ppm		Ratio		Ratio		Ratio		Ratio		Ratio		Age (Ma)	
															207Pb Corr.	
	Pb	Th	U	Th/U	U238/Pb206	1s	Pb207/Pb206	1s	Pb207/U235	1s	Pb206/U238	1s	Pb208/Th232	1s	Pb208/Th232	1s
PA-03-09	1.2	503	10.4	48	98.0	3.3	0.1916	0.0109	0.2690	0.0132	0.01020	0.00034	0.00254	0.00007	51.2	1.5
PA-03-10	4.6	2074	12.9	161	84.3	2.4	0.1845	0.0084	0.3013	0.0119	0.01186	0.00034	0.00252	0.00005	50.9	1.0
PA-03-11	4.4	1945	14.6	133	86.5	2.6	0.2481	0.0110	0.3952	0.0147	0.01156	0.00035	0.00255	0.00005	51.5	1.1
PA-03-12	4.1	1845	13.0	142	102.0	3.1	0.0714	0.0051	0.0965	0.0064	0.00980	0.00030	0.00253	0.00005	51.1	1.0
PA-03-13	3.8	1698	12.6	135	108.7	3.8	0.0931	0.0070	0.1179	0.0081	0.00920	0.00032	0.00254	0.00005	51.3	1.1
PA-03-14	3.3	1432	13.7	105	96.9	2.8	0.1439	0.0072	0.2045	0.0091	0.01032	0.00030	0.00254	0.00005	51.3	1.1
PA-03-15	3.0	1359	13.6	100	110.4	3.2	0.0826	0.0050	0.1030	0.0058	0.00906	0.00026	0.00251	0.00005	50.6	1.0
PA-03-16	3.1	1426	12.6	113	110.1	3.5	0.0896	0.0060	0.1120	0.0069	0.00908	0.00029	0.00255	0.00005	51.4	1.1
PA-03-17	1.9	836	11.6	72	111.0	3.3	0.0945	0.0060	0.1173	0.0068	0.00901	0.00027	0.00246	0.00006	49.7	1.1
PA-04-01	14.1	12,804	17.9	715	82.0	2.0	0.0400	0.0028	0.0670	0.0046	0.01219	0.00030	0.00235	0.00004	47.4	0.9
PA-04-02	13.4	12,141	17.6	690	85.5	2.1	0.0360	0.0028	0.0580	0.0044	0.01169	0.00029	0.00236	0.00004	47.7	0.9
PA-04-03	13.7	12,387	16.4	756	69.3	1.9	0.0921	0.0047	0.1829	0.0086	0.01443	0.00039	0.00234	0.00004	47.2	0.9
PA-04-04	11.4	10,636	14.6	728	79.3	2.1	0.0370	0.0030	0.0642	0.0051	0.01261	0.00033	0.00229	0.00004	46.3	0.8
PA-04-05	10.7	9987	13.9	720	83.6	2.1	0.0344	0.0029	0.0566	0.0047	0.01196	0.00030	0.00228	0.00004	46.1	0.8
PA-04-06	12.3	11,064	15.2	727	79.6	2.0	0.0321	0.0027	0.0556	0.0047	0.01257	0.00032	0.00238	0.00004	48.0	0.9
PA-04-07	13.2	11,913	16.1	738	76.8	1.9	0.0529	0.0031	0.0949	0.0053	0.01302	0.00032	0.00236	0.00004	47.7	0.9
PA-04-08	10.9	10,166	14.2	718	84.1	2.1	0.0290	0.0031	0.0474	0.0049	0.01189	0.00030	0.00228	0.00004	46.1	0.8
PA-04-09	10.0	9292	13.0	716	85.8	2.2	0.0343	0.0033	0.0550	0.0052	0.01166	0.00030	0.00230	0.00004	46.4	0.8
PA-04-10	11.5	9983	13.8	726	60.8	1.7	0.2073	0.0090	0.4699	0.0175	0.01646	0.00047	0.00236	0.00004	47.6	0.9
PA-04-11	12.8	11,534	16.9	683	81.3	2.0	0.0781	0.0037	0.1322	0.0059	0.01230	0.00030	0.00237	0.00004	47.8	0.9
PA-04-12	19.6	10,152	14.0	724	81.8	2.0	0.0307	0.0027	0.0516	0.0044	0.01223	0.00030	0.00232	0.00004	46.8	0.9
PA-04-13	11.8	10,860	15.1	717	84.5	2.1	0.0391	0.0030	0.0636	0.0047	0.01183	0.00030	0.00231	0.00004	46.7	0.9
PA-04-14	11.6	10,738	15.1	709	83.3	2.1	0.0316	0.0029	0.0523	0.0047	0.01200	0.00030	0.00231	0.00004	46.7	0.9
PA-04-15	11.5	10,527	14.8	709	43.9	1.1	0.3992	0.0125	1.2508	0.0324	0.02276	0.00058	0.00232	0.00004	46.8	0.9
PA-04-16	11.2	10,145	14.4	704	77.9	1.9	0.0616	0.0036	0.1088	0.0060	0.01283	0.00032	0.00229	0.00004	46.2	0.8
PA-04-17	12.0	10,948	14.8	737	82.6	2.1	0.0352	0.0029	0.0587	0.0048	0.01211	0.00031	0.00228	0.00004	46.1	0.8
PA-04-18	11.7	10,843	14.9	728	80.8	2.0	0.0317	0.0027	0.0539	0.0044	0.01237	0.00031	0.00227	0.00004	45.7	0.8
PA-04-19	11.4	10,671	15.0	712	80.3	2.0	0.0402	0.0027	0.0688	0.0045	0.01245	0.00031	0.00225	0.00004	45.4	0.8

Small slices of the separated grains were embedded in epoxy, sectioned to expose their interiors to the surface, polished and mapped by optical microscopy and backscattered imaging. The analytical procedure for in situ trace elements, including REE, and U–Th–Pb age analysis by LA-ICP-MS and Sm–Nd isotopic measurement by LA-MC-ICP-MS has been described by [27]. Detailed description on the U–Th–Pb methodology can be found in the supplementary material.

4. Results

4.1. Mineralogy and Chemistry

The studied parisites are part of the common calcite/dolomite–emerald–quartz–albite–white mica (Wma) paragenesis, as defined by [20] (stage 2) and [25] (stage 3) and earlier described by [3,28]. Additionally, fluorite, pyrite and baryte are the most common accessory minerals. The wall rocks are graphite-bearing carbonaceous black shales with metasomatized, i.e., albite and pyrite-rich border zones. Whole rock samples collected 1 m away from the veins do not show any alteration either macroscopically or microscopically (see Figure 3). Figure 2a shows the intimate relationship of emeralds, parisite and calcite/dolomite as well as albite in a fractured black shale from the sample locality.

The up to 1.2 cm × 0.6 cm large parisite crystals in samples PA-01contain thin aligned inclusions of baryte, dolomite and calcite (Figure 2b,d, Table 2). Baryte forms the tips of calcite–dolomite inclusions (Figure 2d). In contrast to earlier described possible polycrystalline parisite aggregates [15], the analyzed parisites are monocrystalline, as indicated by back-scattered electron analysis (Figure 2d).

Table 2. Electron microprobe analyses of parisite sample PA 01 and calcite. CO_2 is calculated. B.d.l.: below detection limit.

	PA-01				Calcite	
wt.%	**Core**	**Rim**	**Core**	**Rim**	**Coarse Core**	**Inclusion in Dolomite**
FeO	b.d.l.	b.d.l.	b.d.l.	b.d.l.	0.37	0.39
MgO	b.d.l.	b.d.l.	0.01	b.d.l.	0.06	0.05
CaO	11.40	11.83	11.85	11.42	58.85	59.35
SrO	0.22	0.29	0.28	0.32	0.12	0.13
La_2O_3	14.93	14.58	14.68	15.31	b.d.l	b.d.l.
Ce_2O_3	30.67	29.86	30.23	29.44	0.01	b.d.l
Nd_2O_3	10.81	10.86	10.79	11.84	0.02	b.d.l
Sm_2O_3	1.17	1.17	1.16	1.21	b.d.l	b.d.l
Eu_2O_3	0.54	0.46	0.45	0.54	b.d.l	0.04
Gd_2O_3	1.45	1.46	1.44	1.22	0.01	0.01
Pr_2O_3	3.18	3.21	3.20	3.31	b.d.l	0.02
Y_2O_3	0.74	0.67	0.74	0.50	b.d.l	b.d.l
ThO_2	0.88	1.09	1.26	0.95	u.d.l.	0.02
F	4.58	4.47	4.44	4.52	b.d.l.	b.d.l
Cl	0.02	0.02	0.02	0.02	b.d.l	b.d.l
CO_2	21.33	21.90	21.33	21.29	40.20	39.60

The parisite samples are chemically dominated by Ce (ca. 30 wt.% Ce_2O_3) (parisite-Ce). However, La_2O_3 and Nd_2O_3 reach concentrations of up to 15 wt.% (Table 2). The crystals are fluorine-rich (Table 2) and show subtle variations between the core and rim (Table 2). In addition, they contain rare inclusions of baryte, calcite and dolomite. In contrast to parisite, the inclusions are nearly free of rare-earth elements and fluorine.

4.2. REE Characteristics of the Parisite Environment

Figure 3 shows upper crust normalized REE pattern of the parisite compared to emeralds [26], calcite and the wall rock composition 1m and 1cm away from the veins (Table 3). Emerald, parisite and calcite formed at the same time. In contrast to parisite, as a

pure REE-F-carbonate, emeralds (mean data from [26]) and the wall rock (this study) show relatively low REE concentrations. However, parisite reflects the negative Eu anomaly of the wall rock (Figure 3). In contrast, emeralds display no Eu anomaly and calcite indicate a weak positive Eu anomaly. The REE deflection in the wall rock, with decreasing distance to the parisite-bearing veins, suggests that the black schists are the major source of these elements in parisite.

Table 3. REE concentrations of the wall rock, emeralds and calcite. ICP-OES technique was used for calcite and wall rock analyses. Parisites and emeralds were analyzed by ICP-MS. (1) Emerald values are the mean of seven samples of Alonso-Perez et al. (2021). (2) Upper crustal values are from Rudnik et al. (2003). All concentrations in ppm.

Calcite	La	Ce	Pr	Nd	Sm	Eu	Gd	Tb	Dy	Ho	Er	Tm	Yb	Lu
	5.1	**19.2**	**2.7**	**17.5**	**6**	**5.45**	**30.2**	**6.4**	**40**	**8**	**24**	**3.8**	**26**	**3.5**
Black shale. 1 cm distant	1.9	1.5	0.2	0.8	0.2	0.1	0.6	0.1	0.6	0.1	0.3	0.1	0.4	0.1
Black shale. 1 m distant	9.7	8.3	1.0	3.9	1.2	0.2	1.6	0.3	2.2	0.5	1.7	0.3	2.0	0.4
PA-01 (mean of 18)	82,454	149,385	17,632	65,057	8399	754	4171	327	1153	134	190	11	31	1
PA-02 (mean of 17)	85,103	149,385	17,345	63,535	8064	754	3819	298	1066	126	182	11	31	2
PA-03 (mean of 23)	84,154	150,606	17,178	60,363	7948	700	4516	347	1218	134	181	11	32	3
PA-04 (mean of 13)	85,140	150,606	18,495	69,737	8746	694	4692	322	1048	110	144	8	20	2
Emerald (mean of 7) (1)	0.1774	0.38306	0.0446	0.1695	0.038	0.008	0.032	0.004	0.022	0.003	0.009	0.002	0.012	0.003
Upper crust (2)	31	63	7.1	27	4.7	1	4	0.7	3.9	0.83	2.3	0.3	2	0.31

4.3. Isotopic Data ($^{232}Th/^{208}Pb$ and Sm/Nd)

As shown in Figure 4 and Table 1, the four parisite samples yielded $^{232}Th/^{208}Pb$ ages of 47.88 ± 0.46 Ma (2s, n = 12), 50.13 ± 0.65, Ma (2s, n = 17), 50.93 ± 0.52 (2s, n = 17) and 46.77 ± 0.36 Ma (2s, n = 19), for samples PA-01, PA-02, PA-03 and PA-04, respectively. The ages are very similar and cluster around 47 and 50 Ma.

Our analysis demonstrates that precise and accurate U–Th–Pb ages can be obtained from parisite after common ^{207}Pb correction. A higher precision date was obtained with the $^{232}Th/^{208}Pb$ ratio rather than with the U–Pb ratio because of the relatively higher content of Th than U in the samples (see Table 1). Parisite has not been dated before; therefore, the potential of this mineral as a U–Th–Pb geochronometer has not been properly investigated. According to this study, parisite has sufficient concentrations of U and Th (Table 1), which makes it possible to precisely measure the U–Th–Pb isotopic composition by in situ (laser or ion probe) technique [27]. It is important to note that the U–Pb decay system with two independent decay chains ($^{206}Pb/^{238}U$, $^{207}Pb/^{235}U$), offers an internal check on a closed system. This is the main advantage of the U–Pb system over the Th–Pb system ($^{208}Pb/^{232}Th$) (see [27] for more details). However, our dating of Colombian parisite produced more precise results with the Th–Pb system than with the U–Pb.

The intermediate daughter isotope ^{230}Th decays with a half-life of ~7500 a in the ^{238}U–^{206}Pb decay chain. Our samples incorporated excess ^{230}Th during crystallization. This excess ^{230} Th will completely decay into ^{206}Pb, which is not the daughter isotope of the ^{238}U within the mineral [29]. Thus, the U–Pb method is not applicable to parisite grains with relatively high Th/U ratios [30]. This problem does not exist for the Th–Pb system because each of the intermediate nuclei of the ^{232}Th–^{208}Pb decay chain have a very short half-life. Hence, we used the Th–Pb age rather than the U–Pb age to date the parisite samples in the present study.

Additionally, the Sm and Nd concentrations and Nd isotopic ratios are listed in Table 4 and plotted in Figure 4. The data points display some differences for sample PA-02 compared to the other samples in the $^{147}Sm/^{144}Nd$ versus $^{143}Nd/^{144}Nd$ diagram (Supplementary Figure S1, Table 4) with higher $^{147}Sm/^{144}Nd$. The difference affecting sample PA-02 might be related to an ablation bias due to differing volatilities of Sm and Nd. The initial $\varepsilon Nd_{(t)}$ is very similar (−8.10 to −8.90), indicating similar genetic evolution of rock chemistry.

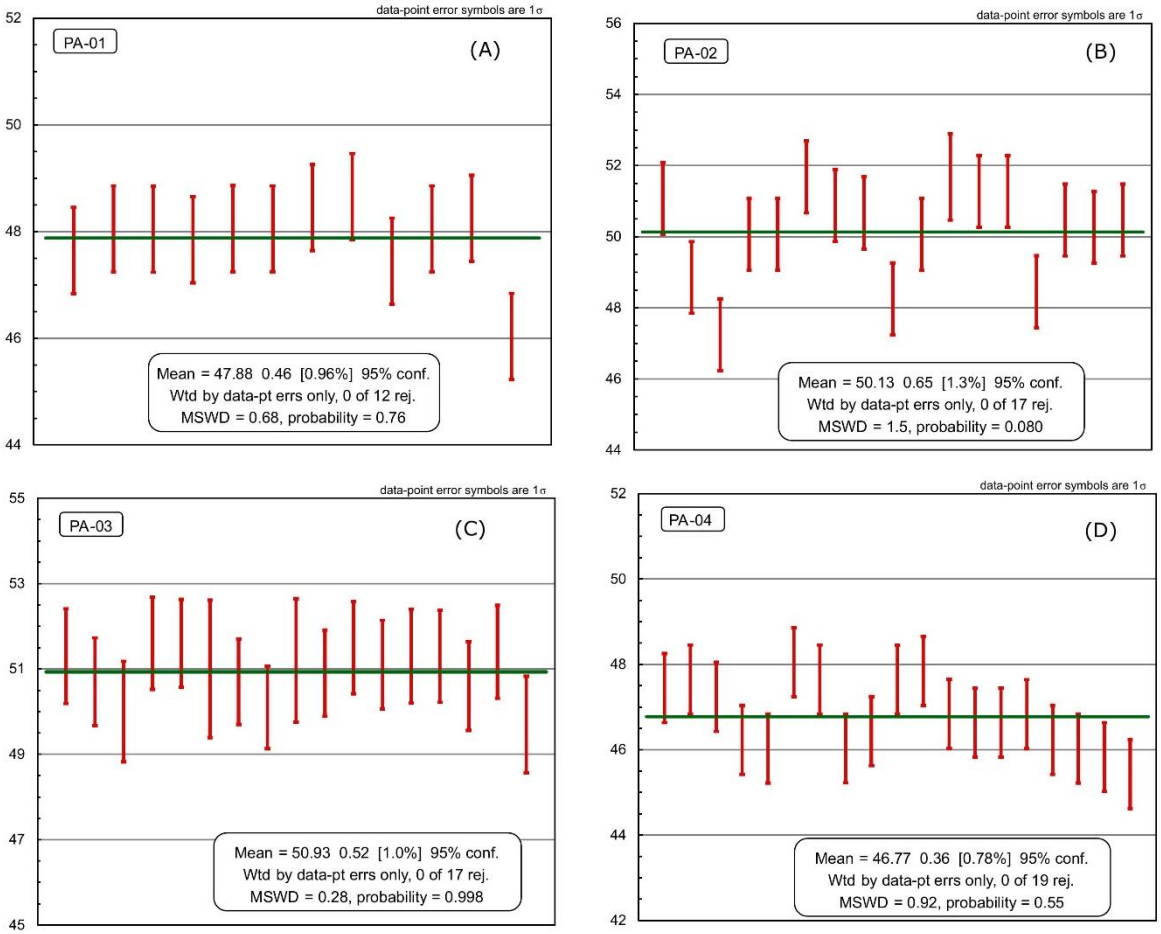

Figure 4. Mean In situ Th–Pb ages obtained by LA-ICP-MS for parisite samples PA-01 (**A**), PA-02 (**B**), PA-03 (**C**) and PA-04 (**D**).

Table 4. 147Sm/144Nd, 143Nd/144Nd and 145Nd/144Nd data.

Sample	Age (Ma)	2s	147Sm/144Nd	2se	143Nd/144Nd	2se	145Nd/144Nd	2se	$e_{Nd}(t)$
PA-01									
PA-01 01	47.9	1	0.0791	0.0004	0.512147	0.000026	0.348406	0.000027	−8.86
PA-01 02	47.9	1	0.0779	0.0001	0.512156	0.000030	0.348391	0.000026	−8.68
PA-01 03	47.9	1	0.0782	0.0002	0.512137	0.000027	0.348377	0.000027	−9.05
PA-01 04	47.9	1	0.0797	0.0003	0.512144	0.000030	0.348401	0.000029	−8.91
PA-01 05	47.9	1	0.0790	0.0002	0.512163	0.000030	0.348381	0.000025	−8.55
PA-01 06	47.9	1	0.0782	0.0003	0.512136	0.000027	0.348393	0.000027	−9.07
PA-01 07	47.9	1	0.0784	0.0002	0.512146	0.000031	0.348385	0.000026	−8.87
PA-01 08	47.9	1	0.0776	0.0001	0.512164	0.000030	0.348405	0.000026	−8.53
PA-01 09	47.9	1	0.0768	0.0001	0.512154	0.000030	0.348398	0.000031	−8.71
PA-01 10	47.9	1	0.0796	0.0002	0.512132	0.000028	0.348385	0.000024	−9.17
PA-01 11	47.9	1	0.0781	0.0002	0.512155	0.000029	0.348383	0.000026	−8.69
PA-01 12	47.9	1	0.0792	0.0003	0.512166	0.000028	0.348409	0.000025	−8.49
PA-01 13	47.9	1	0.0795	0.0002	0.512172	0.000028	0.348389	0.000025	−8.37
PA-01 14	47.9	1	0.0790	0.0003	0.512162	0.000029	0.348379	0.000023	−8.57
PA-01 15	47.9	1	0.0794	0.0002	0.512168	0.000031	0.348402	0.000025	−8.45
PA-01 16	47.9	1	0.0802	0.0003	0.512166	0.000030	0.348383	0.000027	−8.50
PA-01 17	47.9	1	0.0784	0.0002	0.512148	0.000028	0.348385	0.000025	−8.84
PA-01 18	47.9	1	0.0790	0.0003	0.512167	0.000031	0.348408	0.000025	−8.48
PA-01 19	47.9	1	0.0784	0.0002	0.512158	0.000030	0.348390	0.000029	−8.65
PA-01 20	47.9	1	0.0789	0.0002	0.512114	0.000026	0.348401	0.000026	−9.50
Mean	47.9	1	0.0787	0.0016	0.512153	0.000030	0.348393		−8.75

Table 4. *Cont.*

Sample	Age (Ma)	2s	147Sm/144Nd	2se	143Nd/144Nd	2se	145Nd/144Nd	2se	$e_{Nd}(t)$
PA-02									
PA-02 01	50.1	1	0.0855	0.0001	0.512164	0.000031	0.348377	0.000027	−8.53
PA-02 02	50.1	1	0.0833	0.0004	0.512130	0.000030	0.348385	0.000024	−9.19
PA-02 03	50.1	1	0.0849	0.0003	0.512143	0.000030	0.348368	0.000026	−8.94
PA-02 04	50.1	1	0.0834	0.0004	0.512173	0.000033	0.348398	0.000027	−8.35
PA-02 05	50.1	1	0.0800	0.0004	0.512181	0.000031	0.348369	0.000028	−8.17
PA-02 06	50.1	1	0.0802	0.0004	0.512147	0.000032	0.348377	0.000027	−8.83
PA-02 07	50.1	1	0.0776	0.0002	0.512174	0.000028	0.348341	0.000030	−8.29
PA-02 08	50.1	1	0.0788	0.0001	0.512165	0.000029	0.348382	0.000033	−8.47
PA-02 09	50.1	1	0.0781	0.0003	0.512121	0.000034	0.348376	0.000034	−9.33
PA-02 10	50.1	1	0.0875	0.0001	0.512165	0.000033	0.348389	0.000030	−8.54
PA-02 11	50.1	1	0.0819	0.0005	0.512131	0.000031	0.348385	0.000024	−9.16
PA-02 12	50.1	1	0.0848	0.0003	0.512162	0.000032	0.348384	0.000026	−8.57
PA-02 13	50.1	1	0.0862	0.0001	0.512169	0.000031	0.348406	0.000023	−8.44
PA-02 14	50.1	1	0.0765	0.0001	0.512139	0.000031	0.348390	0.000033	−8.97
PA-02 15	50.1	1	0.0769	0.0001	0.512152	0.000031	0.348358	0.000029	−8.72
PA-02 16	50.1	1	0.0776	0.0001	0.512148	0.000030	0.348369	0.000032	−8.80
PA-02 17	50.1	1	0.0788	0.0003	0.512137	0.000033	0.348365	0.000033	−9.03
PA-02 18	50.1	1	0.0775	0.0001	0.512156	0.000035	0.348384	0.000030	−8.63
PA-02 19	50.1	1	0.0773	0.0001	0.512130	0.000031	0.348388	0.000030	−9.15
PA-02 20	50.1	1	0.0770	0.0000	0.512139	0.000033	0.348374	0.000031	−8.96
Mean	50.1	1	0.0807	0.0072	0.512151	0.000035	0.348378		−8.75
PA-03									
PA-03 01	50.9	1	0.0802	0.00010	0.512194	0.000031	0.348415	0.000009	−7.91
PA-03 02	50.9	1	0.0798	0.00010	0.512178	0.000040	0.348411	0.000011	−8.22
PA-03 03	50.9	1	0.0783	0.00010	0.512188	0.000044	0.348408	0.000012	−8.01
PA-03 04	50.9	1	0.0797	0.00010	0.512169	0.000042	0.348409	0.000011	−8.39
PA-03 05	50.9	1	0.0796	0.00010	0.512180	0.000048	0.348413	0.000011	−8.17
PA-03 06	50.9	1	0.0791	0.00010	0.512184	0.000046	0.348410	0.000011	−8.09
PA-03 07	50.9	1	0.0810	0.00010	0.512195	0.000045	0.348400	0.000012	−7.89
PA-03 08	50.9	1	0.0804	0.00010	0.512195	0.000043	0.348404	0.000013	−7.89
PA-03 09	50.9	1	0.0798	0.00010	0.512200	0.000046	0.348408	0.000012	−7.79
PA-03 10	50.9	1	0.0785	0.00010	0.512174	0.000041	0.348414	0.000010	−8.28
PA-03 11	50.9	1	0.0809	0.00010	0.512199	0.000047	0.348410	0.000012	−7.81
PA-03 12	50.9	1	0.0807	0.00010	0.512179	0.000035	0.348407	0.000010	−8.20
PA-03 13	50.9	1	0.0785	0.00010	0.512173	0.000039	0.348407	0.000010	−8.30
PA-03 14	50.9	1	0.0809	0.00010	0.512188	0.000036	0.348410	0.000011	−8.03
PA-03 15	50.9	1	0.0783	0.00010	0.512174	0.000040	0.348424	0.000011	−8.28
PA-03 16	50.9	1	0.0792	0.00010	0.512188	0.000042	0.348415	0.000011	−8.02
PA-03 17	50.9	1	0.0793	0.00010	0.512199	0.000046	0.348416	0.000012	−7.80
PA-03 18	50.9	1	0.0792	0.00010	0.512177	0.000034	0.348406	0.000010	−8.23
PA-03 19	50.9	1	0.0806	0.00010	0.512168	0.000039	0.348411	0.000010	−8.42
PA-03 20	50.9	1	0.0797	0.00010	0.512177	0.000038	0.348406	0.000010	−8.23
Mean	50.9	1	0.0797	0.0018	0.512184	0.000021	0.348410		−8.10
PA-04									
PA-04 01	46.8	1	0.0763	0.0000	0.512166	0.000029	0.348401	0.000029	−8.49
PA-04 02	46.8	1	0.0758	0.0000	0.512150	0.000030	0.348400	0.000034	−8.80
PA-04 03	46.8	1	0.0770	0.0001	0.512154	0.000031	0.348388	0.000033	−8.74
PA-04 04	46.8	1	0.0763	0.0001	0.512175	0.000031	0.348404	0.000033	−8.32
PA-04 05	46.8	1	0.0767	0.0001	0.512133	0.000028	0.348417	0.000031	−9.14
PA-04 06	46.8	1	0.0769	0.0001	0.512125	0.000027	0.348408	0.000034	−9.29
PA-04 07	46.8	1	0.0768	0.0001	0.512163	0.000027	0.348411	0.000033	−8.55
PA-04 08	46.8	1	0.0763	0.0001	0.512134	0.000026	0.348393	0.000034	−9.11
PA-04 09	46.8	1	0.0766	0.0000	0.512151	0.000025	0.348403	0.000033	−8.78
PA-04 10	46.8	1	0.0763	0.0000	0.512145	0.000026	0.348395	0.000039	−8.91
PA-04 11	46.8	1	0.0758	0.0000	0.512180	0.000027	0.348418	0.000035	−8.20
PA-04 12	46.8	1	0.0766	0.0001	0.512145	0.000028	0.348404	0.000032	−8.89
PA-04 13	46.8	1	0.0765	0.0000	0.512124	0.000025	0.348390	0.000034	−9.31
PA-04 14	46.8	1	0.0758	0.0000	0.512146	0.000026	0.348399	0.000033	−8.87
PA-04 15	46.8	1	0.0763	0.0001	0.512122	0.000027	0.348405	0.000035	−9.34
PA-04 16	46.8	1	0.0762	0.0001	0.512144	0.000026	0.348395	0.000034	−8.92
PA-04 17	46.8	1	0.0759	0.0000	0.512132	0.000025	0.348395	0.000035	−9.15
PA-04 18	46.8	1	0.0774	0.0001	0.512135	0.000025	0.348401	0.000038	−9.10
PA-04 19	46.8	1	0.0768	0.0000	0.512144	0.000027	0.348399	0.000038	−8.93
PA-04 20	46.8	1	0.0765	0.0001	0.512133	0.000027	0.348390	0.000038	−9.14
Mean	46.8	1	0.0764	0.0009	0.512145	0.000033	0.348401		−8.90

5. Discussion

The two large emerald districts in Colombia, especially that of Muzo, are famous for their high-quality crystals, and for their unique genesis. In contrast to other great emerald deposits worldwide, such as in Brazil [26], which are due to metasomatic interaction between acid magmatism and basic–ultrabasic rocks, the Colombian ones are formed by low-temperature hydrothermal brines that provide the necessary elements from the wall rocks that are of sedimentary origin. Flat crustal normalized REE and incompatible trace element patterns of emeralds [26], as well as the REE leaching of the wall rock (this study), support the theory of a non-magmatic controlled environment to form parisite.

The motivation to carry out the present study comes from the observation that parisite and emerald grew almost simultaneously in the western district. Our new and well constrained Th–Pb ages of parisite and, by inference, also for the emeralds of the Muzo region of approximately 47–51 Ma, reduces the confusion stemming from different ages for the Colombian emerald deposits. Cheilletz et al. [6] and Svadlenak [7]) describe calculated Ar/Ar white-mica ages of 32–30 Ma and 62 Ma for the western zone and Cheilletz et al. [23] describe ages of 65 Ma for the eastern zone. The $^{87}Sr/^{86}Sr$ in the $^{87}Rb/^{86}Sr$ system calculations [6] gave ages around 61 Ma for the eastern zone and 67 Ma for the western zone of the Eastern Cordillera. Except for the Rb/Sr data, the ages are derived from white micas that are not proven to be co-genetic. The difference between the Rb–Sr emerald ages and the Th–Pb ages of parisite are not well understood.

The originally estimated differences of Ar/Ar ages of white micas and Rb/Sr ages of emeralds of the eastern and western zones were up to 30 Ma [6,23,24]. The new Th–Pb data from the western domain, which grew simultaneously with the emerald, reduces the age difference to ca 10 Ma. Unfortunately, there are no known parisite occurrences in the eastern emerald belt to compare the new ages. The tectonic scenario during the genesis of the emerald deposit should be reevaluated in the framework of the known mica ages. The new age of the western deposit suggests a possible revision to a similar tectonic and geodynamic situation as in the east, i.e., during a thin-skinned extensional tectonic period. However, the formation of both emerald zones is clearly of Paleogene age.

6. Conclusions

Th–Pb isotopic analysis of parasite has been proven to be a reliable geochronological tool in dating primary geological or overprinted systems where common datable minerals (e.g., Ar–Ar in Mica, U–Pb in zircon) are lacking. The parisites and, therefore, the emeralds in the world-famous Muzo area are now dated to an age between 47 and 51 Ma. This is in contrast to former estimates, which are mainly based on non-syngenetic minerals such as white mica or the Rb/Sr data of emeralds. The new ages require a new structural model which is beyond the scope of this study. Assuming these ages, either an extensive tectonic regime in the western zone similar to that in the eastern zone must be expected, or an emerald formation in a different tectonic setting, as proposed so far (e.g., [24]).

Supplementary Materials: The following supporting information can be downloaded at: https://www.mdpi.com/article/10.3390/min12101232/s1, Figure S1: Plot of $^{147}Sm/^{144}Nd$ vs. $^{143}Nd/^{144}Nd$ for parisite samples.docx [31–38].

Author Contributions: Conceptualization, U.A., Y.R.-A. and J.F.-L.; Project administration: Y.R.-A., U.A. and T.H.; Writing and editing: U.A., Y.R.-A., T.H. and J.F.-L.; Trace element analytics and data handling: Microprobe: SEM/EDX: C.G., J.A. and U.A.; Mass spectrometry: Y.Y.; Sampling and field work: J.F.-L., F.C.-L., A.G.-P. and F.C.-L.; Literature research: J.F.-L. and U.A. All authors have read and agreed to the published version of the manuscript.

Funding: U.A. was funded by the University of Potsdam grant KoUP-program. Y.R.-A. acknowledges financial support to the FAPA funding from Universidad de los Andes. Y.Y.-H. acknowledges financial support by the Natural Science Foundation of China.

Acknowledgments: We would like to specially thank all the traditional miners in Colombia, who invited us not only to their mines but also to their homes. Thanks to them, we were able to enter their mines, some of them very small and with few resources but with the great dream of finding the big emerald that will get them out of their poverty and needs. (41525012). We thank C. Kallich for drawing Figure 1 and A.E. Concha Perdomo for the wonderful support during the stays in Colombia (U.A.).

Conflicts of Interest: The authors declare no conflict of interest.

References

1. Giuliani, G.; Groat, L.A.; Marshall, D.; Fallick, A.E.; Branquet, Y. Emerald Deposits: A Review and Enhanced Classification. *Minerals* **2019**, *9*, 105. [CrossRef]
2. Giuliani, G.; Cheilletz, A.; Baker, J.; Arhan, T. Evaporitic Origin of the Patern Brines of Colombian Emeralds: Fluid Inclusion and Sulphur Isotopic Evidences. *Arch. Mineral.* **1993**, *49*, 82–84.
3. Oppenheim, V. The Muzo Emerald Zone, Colombia, S.A. *Econ. Geol.* **1948**, *43*, 31–38. [CrossRef]
4. Giuliani, G.; France-Lanord, C.; Cheilletz, A.; Coget, P.; Branquet, Y.; Laumomnier, B. Sulfate Reduction by Organic Matter in Colombian Emerald Deposits: Chemical and Stable Isotope (C, O, H) Evidence. *Econ. Geol.* **2000**, *95*, 1129–1153. [CrossRef]
5. Romero-Ordoñez, F.H.; Schultz-Güttler, R.A.; Kogi, K. Geoquímica Del Rubidio-Estroncio y Edad de Las Esmeraldas Colombianas. *Geol. Colomb.* **2000**, *25*, 221–239.
6. Cheilletz, A.; Féraud, G.; Giuliani, G.; Rodriguez, C. Time-Pressure and Temperature Constraints on the Formation of Colombian Emeralds; an 40 Ar/39 Ar Laser Microprobe and Fluid Inclusion Study. *Econ. Geol.* **1994**, *89*, 361–380. [CrossRef]
7. Svadlenak, E. 40 Ar/39 Ar Ages and Trace Element Variations in Colombian Emeralds. Unpublished BSC Honors College Thesis Oregon State University, 2015.
8. Bunsen, R. Ueber Den Parisit, Ein Neues Cerfossil. *Wöhler und Liebig's Annalen* **1854**, 147–156. [CrossRef]
9. Lleras Codazzi, R. *La Contribución al Estudio de Los Minerales de Colombia*; Imprenta nacional: Bogota, Colombia, 1916; p. 17.
10. Cook, R.B. Connoisseur's Choice: Parisite Muzo District, Colombia. *Rocks Miner.* **2000**, *75*, 250–252. [CrossRef]
11. Gübelin, E.; Koivula, J. *Photoatlas of Inclusions in Gemstones*; ABC Edition: Zuerich, Switzerland, 1986; p. 532.
12. Ottaway, T.; Wicks, F.; Bryndzia, L.; Kyser, T.; Spooner, E. Formation of the Muzo Hydrothermal Emerald Deposit in Colombia. *Nature* **1994**, *369*, 552–554. [CrossRef]
13. Donnay, G.; Donnay, J. The Crystallography of Bastnaesite, Parisite, Roentgenite, and Synchisite. *Am. Mineral. J. Earth Planet. Mater.* **1953**, *38*, 932–963.
14. Zeug, M.; Nasdala, L.; Ende, M.; Habler, G.; Hauzenberger, C.; Chanmuang, N.C.; Škoda, R.; Topa, D.; Wildner, M.; Wirth, R. The Parisite–(Ce) Enigma: Challenges in the Identification of Fluorcarbonate Minerals. *Min. Pet.* **2021**, *115*, 1–19. [CrossRef]
15. Artel, J.; Altenberger, U.; Günter, C.; Fernadez-Lamus, J. *The Formation of Rare Earth Mineral Pariste in Emerald Bearing Carbonate Veins of Muzo/Colombia*; German Mineralogical Assoziation (DMG): Dresden, Germany, 2014.
16. Fabre, A. La Subsidencia de La Cuenca Del Cocuy (Cordillera Oriental de Colombia) Durante El Cretáceo y El Terciario Inferior. *Primera parte: Estudio cuantitativo de la subsidencia: Geol. Norandina* **1983**, *8*, 22–27.
17. Sarmiento Rojas, L.F. Mesozoic Rifting and Cenozoic Basin Inversion-History of the Eastern Cordillera, Combian Andes. Inferences from Tectonic Models. Ph.D. Thesis, Vrije Universiteit Amsterdam, Amsterdam, The Netherlands, 2002.
18. Mora, A.; Gaona, T.; Kley, J.; Montoya, D.; Parra, M.; Quiroz, L.I.; Reyes, G.; Strecker, M.R. The Role of Inherited Extensional Fault Segmentation and Linkage in Contractional Orogenesis: A Reconstruction of Lower Cretaceous Inverted Rift Basins in the Eastern Cordillera of Colombia. *Basin Res.* **2009**, *21*, 111–137. [CrossRef]
19. Fabre, A. Tectonique et Génération d'hydrocarbures: Un Modèle de l'évolution de La Cordillère Orientale de Colombie et Du Bassin Des Llanos Pendant Le Crétacé et Le Tertiaire. *Arch. Sci. Genève* **1987**, *40*, 145–190.
20. Cheilletz, A.; Giuliani, G. The Genesis of Colombian Emeralds: A Restatement. *Mineral. Deposita* **1996**, *31*, 359–364. [CrossRef]
21. Vásquez, M.; Altenberger, U. Mid-Cretaceous Extension-Related Magmatism in the Eastern Colombian Andes. *J. S. Am. Earth Sci.* **2005**, *20*, 193–210. [CrossRef]
22. Branquet, Y.; Laumonier, B.; Cheilletz, A.; Giuliani, G. Emeralds in the Eastern Cordillera of Colombia: Two Tectonic Settings for One Mineralization. *Geology* **1999**, *27*, 597–600. [CrossRef]
23. Cheilletz, A.; Giuliani, G.; Branquet, Y.; Laumonier, B.; Sanchez, A.; Féraud, G.; Arhan, T. Datation K-Ar et 40Ar/39Ar à 65 ± 3 Ma Des Gisements d'émeraude Du District de Chivor-Macanal: Argument En Faveur d'une Déformation Précoce Dans La Cordillère Orientale de Colombie. *C. R. Acad. Sci. II* **1997**, *324*, 369–377.
24. Laumonier, A.B.; Branquet, Y.; Cheilletz, A.; Giuliani, G.; Rueda, F. Mise en évidence d'une tectonique compressive. Eocène-Oligocène dans l'Ouest de la Cordillère orientale de Colombie d'après la structure en duplex des gisements d'émeraude de et Coscuez. *Académie Des Sci. Comptes Rendus* **1996**, *323*, 705–712.
25. Banks, D.; Giuliani, G.; Yardley, B.W.; Cheilletz, A. Emerald Mineralisation in Colombia: Fluid Chemistry and the Role of Brine Mixing. *Miner. Depos.* **2000**, *35*, 699–713. [CrossRef]
26. Alonso-Perez, R.; Day, J.M.D. Rare Earth Element and Incompatible Trace Element Abundances in Emeralds Reveal Their Formation Environments. *Minerals* **2021**, *11*, 513. [CrossRef]

27. Yang, Y.; Wu, F.; Li, Q.; Rojas-Agramonte, Y.; Yang, J.; Li, Y.; Ma, Q.; Xie, L.; Huang, C.; Fan, H. In Situ U-Th-Pb Dating and Sr-Nd Isotope Analysis of Bastnäsite by LA-(MC)-ICP-MS. *Geostand. Geoanalytical Res.* **2019**, *43*, 543–565. [CrossRef]
28. Hall, M.L. *Mineralogía y Geoquímica de Las Vetas Esmeraldíferas de Muzo-Departamento de Boyacá Con Implicaciones En La Prospección Futura de Esmeraldas En Otras Partes de Colombia*; Universidad Nacional: Bogota, Colombia, 1976; p. 276.
29. Schärer, U. The Effect of Initial230Th Disequilibrium on Young UPb Ages: The Makalu Case, Himalaya. *Earth Planet. Sci. Lett.* **1984**, *67*, 191–204. [CrossRef]
30. Ling, X.; Li, Q.; Liu, Y.; Yang, Y.; Tang, G.; Li, X. In Situ SIMS Th–Pb Dating of Bastnaesite: Constraint on the Mineralization Time of the Himalayan Mianning–Dechang Rare Earth Element Deposits. *J. Anal. At. Spectrom.* **2016**, *31*, 1680–1687. [CrossRef]
31. Sal'Nikova, E.; Yakovleva, S.; Nikiforov, A.; Kotov, A.; Yarmolyuk, V.; Anisimova, I.; Sugorakova, A.; Plotkina, Y.V. *Bastnaesite: A Promising U-Pb Geochronological Tool*; Springer Nature BV: Berlin/Heidelberg, Germany, 2010; Volume 430, p. 134.
32. Ludwig, K. A Geochronological Toolkit for Microsoft Excel. *Isoplot* **2003**, *3*, 1–70.
33. Griffin, W. GLITTER: Data Reduction Software for Laser Ablation ICP-MS. *Laser Ablation ICP-MS Earth Sci. Curr. Pract. Outst. Issues* **2008**, *2008*, 308–311.
34. Chew, D.; Petrus, J.; Kamber, B. U–Pb LA–ICPMS Dating Using Accessory Mineral Standards with Variable Common Pb. *Chem. Geol.* **2014**, *363*, 185–199. [CrossRef]
35. Stacey, J.T.; Kramers, J.D. Approximation of Terrestrial Lead Isotope Evolution by a Two-Stage Model. *Earth Planet. Sci. Lett.* **1975**, *26*, 207–221. [CrossRef]
36. Yang, Y.; Sun, J.; Xie, L.; Fan, H.; Wu, F. In Situ Nd Isotopic Measurement of Natural Geological Materials by LA-MC-ICPMS. *Chin. Sci. Bull.* **2008**, *53*, 1062–1070. [CrossRef]
37. Dubois, J.; Retali, G.; Cesario, J. Isotopic Analysis of Rare Earth Elements by Total Vaporization of Samples in Thermal Ionization Mass Spectrometry. *Int. J. Mass Spectrom. Ion Process.* **1992**, *120*, 163–177. [CrossRef]
38. Isnard, H.; Brennetot, R.; Caussignac, C.; Caussignac, N.; Chartier, F. Investigations for Determination of Gd and Sm Isotopic Compositions in Spent Nuclear Fuels Samples by MC ICPMS. *Int. J. Mass Spectrom.* **2005**, *246*, 66–73. [CrossRef]